pubs.acs.org/Biomac

Article

Dual-Responsive Ultrathin Peptoid Nanofibers Assembled from Amphiphilic Alternating Peptoids with an Integration of Azobenzene and Histamine Moieties

Mingyu Ding, Qianyu Jiang, Pengchao Wu, Pengliang Sui, Zichao Sun, Xiaoling Yang,* Haibao Jin,* and Shaoliang Lin*

Cite This: Biomacromolecules 2025, 26, 2750−2758

Read Online

ACCESS | Metrics & More | Article Recommendations | Supporting Information

ABSTRACT: Ultrathin organic nanofibers (UTONFs) have favorable potential as emerging nanomaterials due to their large aspect ratio, lightweight nature, and mechanical flexibility. Achieving dual stimuli-responsive UTONFs is necessary to satisfy the on-demand requirements of smart and miniature devices but remains challenging. Herein, amphiphilic alternating peptoids (AAPs) modified with azobenzene and histamine groups were successfully synthesized using the solid-phase submonomer synthesis technique. Following subsequent solution self-assembly, photo/CO_2 dual-responsive ultrathin peptoid nanofibers (UTPNFs) with a diameter of ∼1.8 nm and a length of up to several micrometers were generated based on the pendant hydrophobic conjugate stacking mechanism. The photoisomerization of azobenzene was accountable for the reversible transformation from UTPNFs to spherical micelles (∼60 nm) under recyclable light irradiation. Owing to the protonation and the resulting electrostatic repulsion interaction, both UTPNFs and spherical micelles displayed a reversible variation in shape and physicochemical properties, including the size, diameter, zeta potential, and pH. Our work offers prospective guidance on the construction of dual-responsive ultrathin organic nanofibers with controllable shape transformation and performance transition.

1. INTRODUCTION

Stimuli-responsive organic nanofibers (ONFs), as an attractive class of intelligent nanomaterials, possess unique physical and chemical traits, including high specific surface area, significant strength, low density, and mechanical flexibility.[1−4] Stimuli-responsive ONFs are also capable of significant structural or performance transitions dynamically in response to external stimuli such as temperature, pH, ions, electromagnetic fields, etc.[5−7] These attributes and reversible changes facilitate the potential use of stimuli-responsive ONFs for a variety of applications, such as catalysis, sensors, electronics, optics, biomedicine, therapeutics, soft robots, and tissue engineering.[8−12] Crucial considerations toward these stimuli-responsive ONFs are green cleaning, precise spatial and temporal modulation, being free of contamination, and high reversibility and recyclability. Hence, noninvasive stimuli-responsive ONFs are emerging as prospective candidates for a variety of applications. Among them, photoresponsive ONFs offer a promising and favorable platform capable of attractive superiorities in tunable wavelengths, programmable activation or deactivation of signals, noncontact operation, and spatial selectivity.[13,14] For instance, the photoisomerization characteristic of azobenzene and its derivatives promotes the integration and development of azobenzene-based ONFs with a dynamic structural transformation and the resulting performance reversibility.[15−17] Additionally, gas molecules can serve as another intriguing stimulus trigger to fabricate functional ONFs owing to their excellent recyclability and noncontamination toward systems.[18] Particularly, CO_2-responsive ONFs are gradually arising as promising 1D nanomaterials due to their "green" property, mildness, high efficiency, reversible bonding, and excellent biocompatibility.[19−21] Despite great achievements, the development of multifunctional and ultrathin ONFs is inevitable to meet the growing demands for integrated, intelligent, and miniature devices, spontaneously emerging as a lively research hot topic in the fields of chemistry and materials science.[22−24]

Ultrathin organic nanofibers (UTONFs), as an attractive category of 1D nanomaterials, possess a large-aspect-ratio nanostructure and resulting exceptional superiorities such as high specific surface areas, numerous active sites, mechanical strength, preferable stability, and easy functionalization,

Received: February 10, 2025
Revised: March 16, 2025
Accepted: March 20, 2025
Published: March 27, 2025

https://doi.org/10.1021/acs.biomac.5c00211
Biomacromolecules 2025, 26, 2750−2758

exhibiting various applications in biomedicine and nanotechnology.[25−27] To date, diverse methodologies have been exploited to elaborately produce tailorable UTONFs with diameters spanning from tens of nanometers to micrometers, including template synthesis, gas-phase deposition, self-assembly, and electrostatic spinning.[28−31] Despite great achievements, it remains a tremendous challenge to generate functional UTONFs with a diameter below 10 nm that respond to external stimuli for a dynamic structural/performance transition.[32,33]

In recent decades, the self-assembly of amphiphilic alternating copolymers has offered a powerful bottom-up strategy for preparing ultrathin organic nanomaterials with controllable size, composition, and structures (i.e., vesicles, tubes, fibers, and sheets) owing to the precise hydrophilic−lipophilic balance originating from the periodic arrangement of distinct monomeric constituents in the polymeric backbone.[13,34−36] Among the artificial macromolecular amphiphiles, peptoids (or poly-*N*-substituted glycines), as a representative class of peptidomimetic sequence-controlled polymers, have emerged with increasing attention owing to the programmable and facile synthesis, narrow polydispersity, good solubility, attractive side-chain diversity, favorable environmental stability, and biocompatibility.[37−40] These attributes are attractive to produce 1D ultrathin nanomaterials using the self-assembly of amphiphilic alternating peptoids for use in biomedicine and nanotechnology.[41] For instance, based on the pendant hydrophobic conjugated stacking mechanism, we have reported a series of 1D azobenzene-containing ultrathin ∼2 nm peptoid nanomaterials with a reversible phototriggered structural transition and wide applications in nanocatalysis, light-harvesting, biomedicine, etc.[16,32,42−44] Apart from the monoresponsive modulation, the development of peptoid-based 1D ultrathin nanomaterials with dynamic dual-responsive capacity is necessary to satisfy the growing demands for integrated and miniature devices but remains challenging.

Herein, benefiting from the solid-phase submonomer synthesis technique, we rationally designed and synthesized dual-responsive amphiphilic alternating peptoids (AAPs) with a combination of azobenzene and histamine units. The resulting solution self-assembly was performed to generate micrometer-scale photo/CO_2 dual-responsive ultrathin peptoid nanofibers (UTPNFs) with a diameter of ∼1.8 nm. The as-prepared photo- or CO_2-responsive feature of the as-prepared UTPNFs was systematically assessed by investigating the sequentially reversible structural and performance transition.

2. MATERIALS AND METHODS

2.1. Materials. 4-Amino benzylamine, di-*tert*-butyl dicarbonate, 4-dimethylaminopyridine (DMAP), and bromoacetic acid were purchased from TCI Reagent Co., Ltd.. Acetic acid (HAc), tetrahydrofuran (THF), methanol, dichloromethane (DCM), *N,N′*-diisopropylcarbodiimide (DIC), dimethyl sulfoxide-d_6 (DMSO-d_6), hexane, ethyl acetate, and acetonitrile were purchased from Adamas-beta Reagent Co., Ltd.. Trifluoroacetic acid (TFA), chloroacetic acid, histamine, and nitrobenzene were purchased from Aladdin Reagent. 2-Methoxyethylamine was purchased from Macklin Reagent. Sodium hydroxide, sodium bicarbonate, sodium chloride, anhydrous sodium sulfate, and *N,N*-dimethylformamide were purchased for General Reagent Co., Ltd. 4-Methylpiperidine was purchased from ACROS, and hydrochloric acid was bought from the Sinopharm group. All of the reagents were obtained from commercial sources and used without further purification. Deionized water was collected from a Milli-Q system with a resistance of 18.25 MΩ·cm.

2.2. Synthesis of Amphiphilic Alternating Peptoids (AAPs). The Rink amide resin (100 mg, 0.09 mmol) was used to generate *C*-terminal amide peptoids. In the synthetic procedure, the resins were immersed in a mixture of 20% (v/v) 4-methylpiperidine/*N,N*-dimethylformamide (DMF) to deprotect Fmoc groups, agitated for 40 min, drained, and washed with DMF. Notably, all DMF washes were performed in 3 mL of DMF followed by agitation for 1 min (repeated four times). An acylation reaction was performed by adding 1.5 mL of 0.6 M bromoacetic acid in DMF and 0.4 mL of 50% (v/v) *N,N′*-diisopropylcarbodiimide (DIC)/DMF and agitating for 10 min at room temperature. The mixture was filtered and washed with DMF for five times. The nucleophilic displacement reaction between the bromide groups and different primary amines was implemented by adding the primary amine monomer as a 0.6 M solution in DMF followed by agitation for 30 min at room temperature. The mixture was filtered and washed with DMF for five times. The acylation and displacement steps were repeated until the complete synthesis of the targeted peptoids. During the purification of peptoids, the final crude products were cleaved from the corresponding resins using 95% trifluoroacetic acid in water and agitated at 40 °C for 40 min, filtered, and evaporated under a stream of nitrogen gas. The crude products were dissolved in 1 mL of acetonitrile followed by sedimentation−centrifuge with anhydrous diethyl ether. The obtained crude peptoids were dialyzed and subsequently freeze-dried to obtain solid powders.

2.3. Synthesis of UTPNFs. One micromole of AAP powder was dissolved in a THF/H_2O (v/v = 1:1) mixture to obtain a clear solution, slowly evaporating at 4 °C for the self-assembly to obtain ultrathin peptoid nanofiber (UTPNF) aqueous solution with a final concentration of 2 μmol mL^{-1}. An orange gel-like material was formed after a few days.

2.4. Photoresponsive Ability of UTPNFs. To study the photoresponsive property, both peptoid sequences in THF solution and the aggregates in aqueous solution were irradiated with 365 and 450 nm light from a Uvata UP114 LED lamp for different times. To investigate the morphology transformation from UTPNFs to spherical micelles, 1 mL of the as-prepared UTPNF solution (1 μmol mL^{-1}) was dispersed into 3 mL of DI water. The diluted UTPNF aqueous solution was irradiated with 365 nm for 3 h from a Uvata UP114 LED lamp with a light intensity of 175 mW cm^{-2}. To fulfill the recovery into UTPNFs, 1 mL of THF was added into the spherical micelle aqueous solution followed by irradiation with visible light for 3 h. The incubation for slow evaporation was implemented at 4 °C for 7 days.

2.5. CO_2 Response Testing of UTPNFs and Spherical Micelles. To investigate the CO_2-responsive property, both the aggregates in aqueous solution before and after 365 nm light irradiation from a Uvata UP114 LED lamp were bubbled with CO_2 or N_2 gases, respectively. One milliliter of the as-prepared UTPNF solution (2 μmol mL^{-1}) was dispersed into 3 mL of DI water and stored in a 10 mL glass vial. The diluted UTPNF solution was bubbled with a high-purity CO_2 cylinder for 30 min followed by bubbling with a high-purity N_2 cylinder for 1 h. After irradiation, the spherical micelle assemblies were wrapped in tin foil and maintained in a dark environment to complete the above operations.

2.6. Characterizations. The UV−vis spectra were measured by a UV−vis spectrophotometer (UV-2550, Shimadzu). For characterizing the photoresponsive ability of AAPs and UTPNFs, the AAP solution in THF and UTPNF aqueous solution were irradiated using a high-intensity lamp (Uvata UP114) with 365 nm UV light and 450 nm visible light (intensity: 8.75 mW cm^{-2} for THF solution and 17.5 mW·cm^{-2} for aqueous solution) over different irradiation time intervals. All the samples were analyzed under ambient conditions using quartz cells. TEM measurements were performed on a JEM-1400 JEOL at an accelerating voltage of 100 kV. For TEM measurement, a 2.0 μL drop of the assembly solution was diluted with 5.0 μL of DI water and put onto carbon-coated copper grids for 10 min. The droplet was dried with filter paper. AFM height images were recorded on a Bruker MultiMode 8 at room temperature. To prepare the AFM sample, 2 μL of the UTPNF solution was diluted with DI water and placed onto a freshly cleaved mica substance for 1 min. After removing the solution using filter paper, the mica sample

https://doi.org/10.1021/acs.biomac.5c00211
Biomacromolecules 2025, 26, 2750−2758

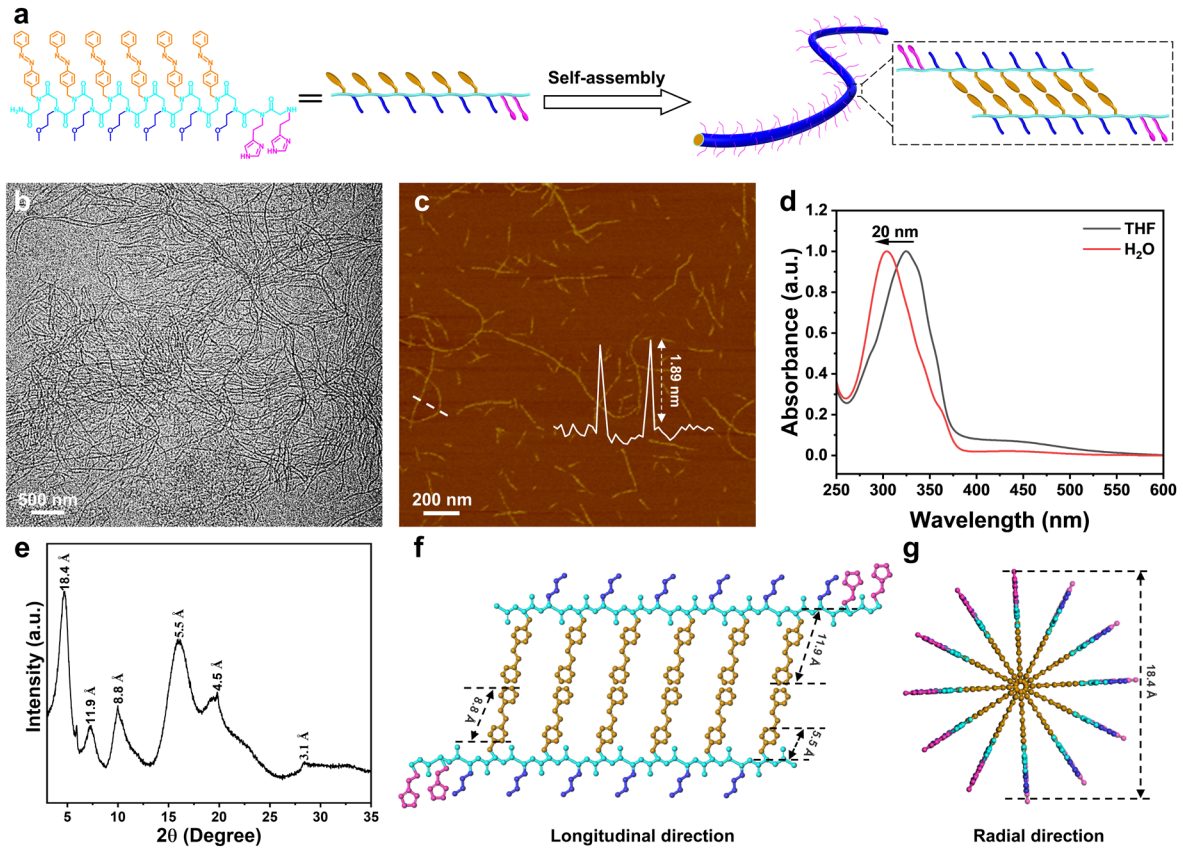

Figure 1. Structural characterizations of UTPNFs assembled from AAPs. (a) Scheme of the self-assembly pathway of AAPs into UTPNFs. (b) TEM image. (c) AFM image. The inset is the corresponding height image demonstrating that the diameter of UTPNFs was around 1.89 nm. (d) Normalized UV−vis spectra. The black line represents AAPs in THF; the red line represents UTPNFs in an aqueous solution. (e) XRD curve. The *d* values corresponding to each peak are calculated by the formula $d = \lambda/2\sin\theta$ (λ = 0.154 nm). (f, g) Conjectural fibrous models for the possible molecular packing of AAPs within UTPNFs viewed from different directions. (f) Longitudinal direction. (g) Radial direction.

was dried using a stream of N_2 gas. The measurements were performed using an X-ray diffractometer with Cu Kα radiation (λ = 1.54 Å) operated in Bragg−Brentano geometry (*/Ultima IV, Nippon Corporation) with a scanning speed of 2°/min. Dynamic light scattering (DLS) and zeta potential patterns were recorded on a Zetasizer Pro with an equilibrated time of 120 s. All the DLS and zeta potential samples were analyzed under ambient conditions and using plastic cells. The pH was recorded on an S210-B instrument (Mettler Toledo).

3. RESULTS AND DISCUSSION

3.1. Self-Assembly of AAPs into UTPNFs. According to the feasible solid-phase submonomer synthesis method, functional AB-type amphiphilic alternating peptoids of (N_{azo}-*alt*-N_{me})$_6$-N_{his2} (Figure 1a) were elaborately designed and synthesized using six photoresponsive hydrophobic A units of *N*-[(azophenyl)methyl] glycine (N_{azo}), six hydrophilic B units of *N*-(2-methoxyethyl) glycine (N_{me}), and two CO_2-responsive functional units of *N*-(1*H*-imidazole-4-ethyl) glycine (N_{his}) as precursors, respectively. The detailed synthesis and analytic characterizations of the N_{azo} monomer and sequence-defined AAPs are given in the Supporting Information (Schemes S1−S2 and Figures S1−S4).

The resulting AAPs were placed in a mixture of water and tetrahydrofuran (THF) at a volume ratio of 50:50 at 4 °C for 7 days without any disturbance to achieve the evaporation-induced self-assembly. An orange gel-like material containing a large number of homogeneous and free-floating UTPNFs was obtained after the following slow evaporation of THF. The transmission electron microscopy (TEM) technique was initially employed to confirm the morphology of the as-prepared aggregates. TEM images (Figure 1b and Figure S5) demonstrated the successful generation of thread-like UTPNFs with a length of up to several micrometers. Atomic force microscopy (AFM) was further utilized to substantially characterize the structural characterizations of the as-prepared UTPNFs. As shown in Figure 1c, wire-like ultrathin nanofibers with a height of ∼1.89 nm (inset in Figure 1c) were observed, consolidating the successful fabrication of the UTPNFs. Ultraviolet−visible (UV−vis) absorption spectroscopy and powder X-ray diffraction (XRD) were also performed to investigate the meticulous molecular information within these as-prepared UTPNFs. Figure 1d displays the UV−vis spectra of AAPs in THF and UTPNFs in aqueous solution. A 20 nm blue shift from 324 nm (THF) to 304 nm (water) was significantly perceived, indicating the self-assembly of AAPs into ordered UTPNFs and the subsequent formation of *H*-aggregation of azobenzene units within UTPNFs. The XRD curve (Figure 1e) proved the highly crystalline ability of the as-prepared UTPNFs. The first strongest peak at 2θ = 4.8° (d = 18.4 Å) was assignable to the fibrous diameter of the UTPNFs, originating from the ordered stacking of AAPs. Of note, the result was very consistent with the AFM height data (∼1.89 nm). The peaks at 11.9 Å (2θ = 7.4°) and 8.8 Å (2θ = 10.0°) were attributable to the length of hydrophobic N_{azo} pendants and rigid azobenzene units, respectively. Another strong peak

https://doi.org/10.1021/acs.biomac.5c00211
Biomacromolecules 2025, 26, 2750−2758

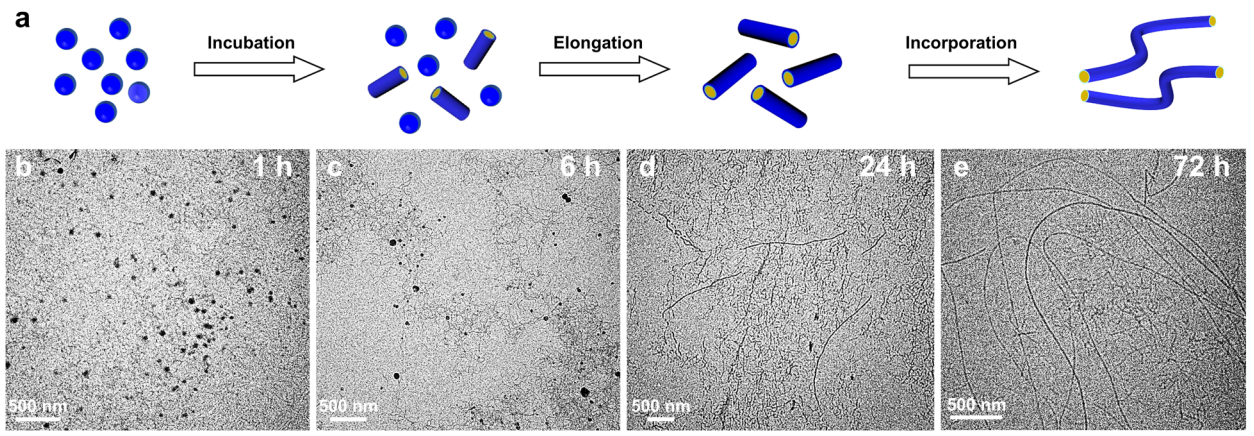

Figure 2. Self-assembly pathway of UTPNFs. (a) Scheme of an evolution procedure of AAPs into UTPNFs. (b–e) Time-dependent TEM images showcasing different self-assembly pathways during the formation of UTPNFs. (b) 1, (c) 6, (d) 24, and (e) 72 h.

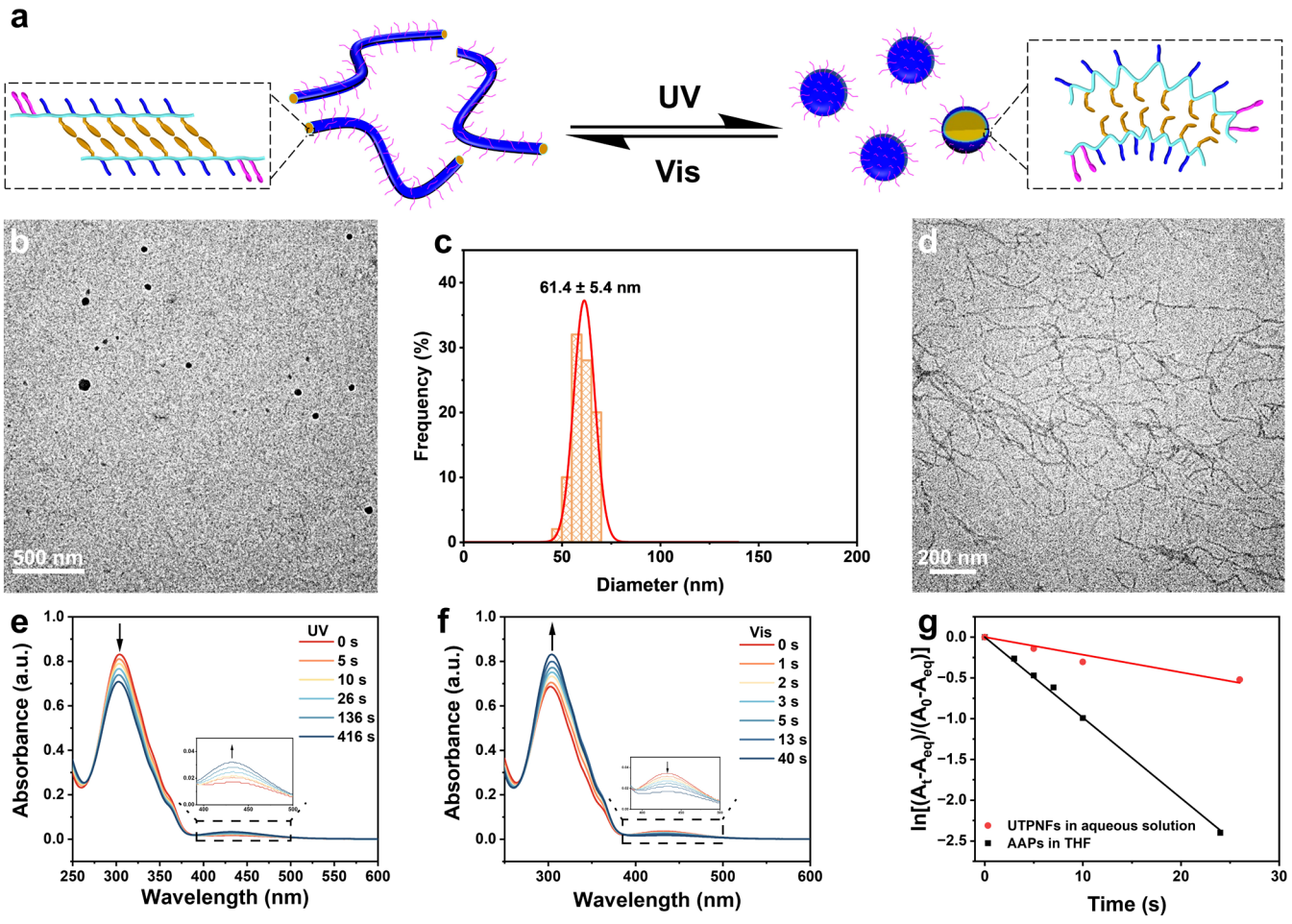

Figure 3. Photoresponsive feature of UTPNFs. (a) Scheme of phototriggered structural transformation from UTPNFs to spherical micelles. (b) TEM image of spherical micelles irradiated by UV light for 3 h. (c) Statistical analysis of the size distribution of spherical micelles (61.4 ± 5.4 nm) by analyzing 50 spherical micelles (d) TEM image of the fully recovered UTPNFs sequentially irradiated by visible light for 3 h. (e) Time-dependent UV–vis absorbance spectra of UTPNFs in aqueous solution under UV irradiation. (f) Subsequent time-dependent UV–vis absorbance spectra under visible light irradiation. (g) Plots of $\ln[(A_t - A_{eq})/(A_0 - A_{eq})]$ as a function of time during the *trans*-to-*cis* photoisomerization of UFPNFs in aqueous solution and AAPs in THF.

(2θ = 16.1°, d = 5.5 Å) corresponded to the length from the first aromatic ring in the N_{azo} side chains to the peptoid backbones. Moreover, the peaks at 4.5 (2θ = 19.8°) and 3.1 Å (2θ = 28.4°) offered significant evidence of the presence of π–π stacking within UTPNFs.

Based on the above-mentioned analysis, we proposed a conjectural fiber-like structural model to reveal the molecular packing of AAPs within the as-prepared UTPNFs (Figure 1f,g). The strong repulsion interaction between the hydrophobic N_{azo} pendants and DI water resulted in meticulous

https://doi.org/10.1021/acs.biomac.5c00211
Biomacromolecules 2025, 26, 2750–2758

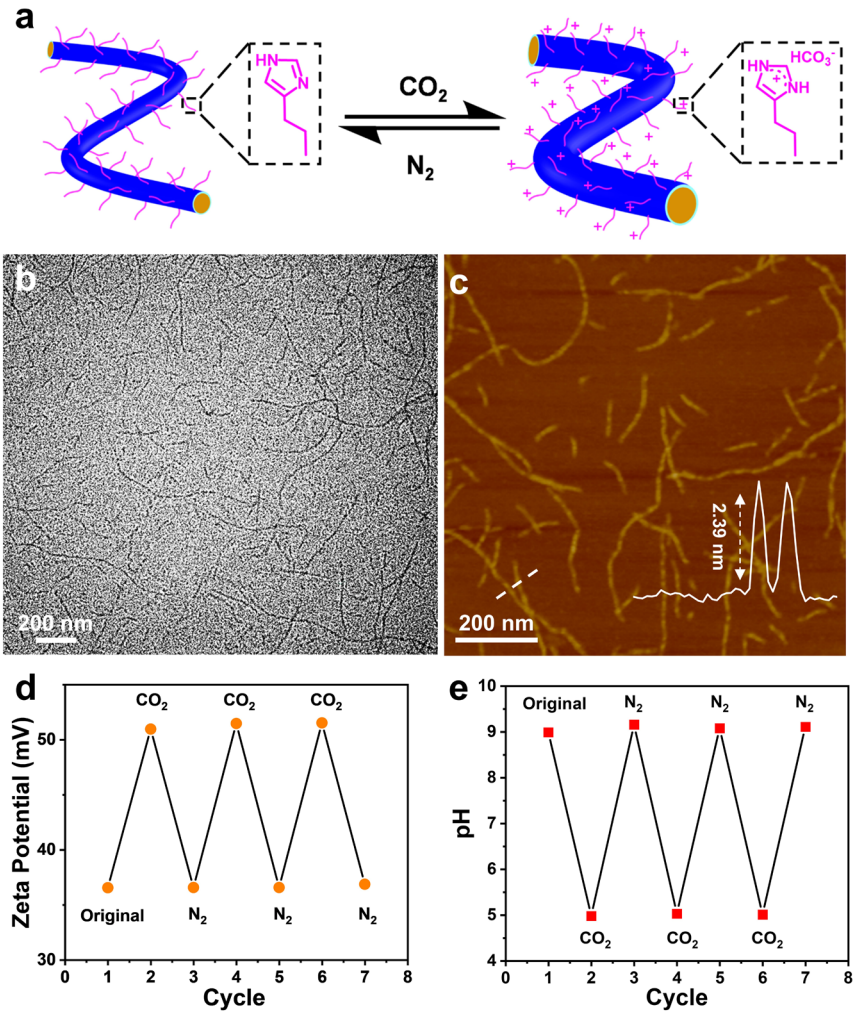

Figure 4. CO_2-responsive feature of UTPNFs. (a) Scheme of size variation for UTPNFs upon the alternating bubbling with CO_2 and N_2 gases. (b–e) Structural characterizations of UTPNFs after bubbling with CO_2 for 30 min. (b) TEM image. (c) AFM image. The inset is the corresponding height image showcasing that the diameter of the newly prepared UTPNFs was ~2.39 nm. (d) Zeta potential changes of the UTPNF aqueous solution. (e) pH changes of the UTPNF aqueous solution.

aggregation into a bilayer cylindrical nanostructure composed of a hydrophobic core and a hydrophilic exterior. The ideal fibrous architecture was beneficial for avoiding the direct contact of N_{azo} with the aqueous surroundings and thus minimizing the surface energy. Notably, the AAPs within UTPNFs were positioned radially along the longitudinal axis as a consequence of the alternating polymeric backbones. Additionally, extensive $\pi-\pi$ stacking among *H*-aggregated *trans*-azobenzene units resulted in the side-by-side stacking of AAPs along the longitudinal direction, subsequently propagating into 1D long-range-ordered UTPNFs at the micrometer level. In other words, the diameter of UTPNFs was highly dependent on the micro-ordered bilayer stacking of hydrophobic pendants of N_{azo} and hydrophilic pendants of N_{me}. Therefore, the pendant hydrophobic conjugate stacking mechanism was accountable for the formation of UTPNFs, similar to other previously produced ultrathin nanomaterials.[16,32,42,43]

To further investigate the elaborate assembly mechanism of UTPNFs, time-dependent TEM images (Figure 2) were collected at different stages of the self-assembly pathway. AAPs initially formed metastable spherical micelles with a diameter of 46.1 ± 6.9 nm (Figure 2a and Figure S6) after complete dissolution in the mixture of THF and water. Following slow evaporation for 6 h, the coexistence of numerous short nanorods and spherical micelles was gradually dissipated in the solution, according to the TEM observation (Figure 2b). The newly apparent nanorods were covered with the external hydrophilic groups to reduce the contact of the N_{azo} with water (Figure 2c), subsequently decreasing the surface energy. Twenty-four hours later, the living short nanorods were actively elongated into short nanowires (Figure 2d), with a complete consumption of spherical micelles. Eventually, the continuous growth or connection resulted in the production of micrometer-scale UTPNFs to minimize the system energy after 72 h incubation (Figure 2e). Of note, the free-standing UTPNFs exhibited favorable stability in aqueous solution over 6 months (Figure S7).

3.2. Photoresponsive Feature of UTPNFs. Photoisomerization characteristic of the azobenzene moiety empowers the relative materials with a reversible photoresponsive capacity. Therefore, the reversible *trans*-to-*cis* transition of the N_{azo} pendants within AAPs under recyclable light irradiation might result in a reversible structural transformation from *trans*-form UTPNFs to *cis*-form spherical micelles (Figure 3a). TEM was utilized to trace the phototriggered structural

https://doi.org/10.1021/acs.biomac.5c00211
Biomacromolecules 2025, 26, 2750–2758

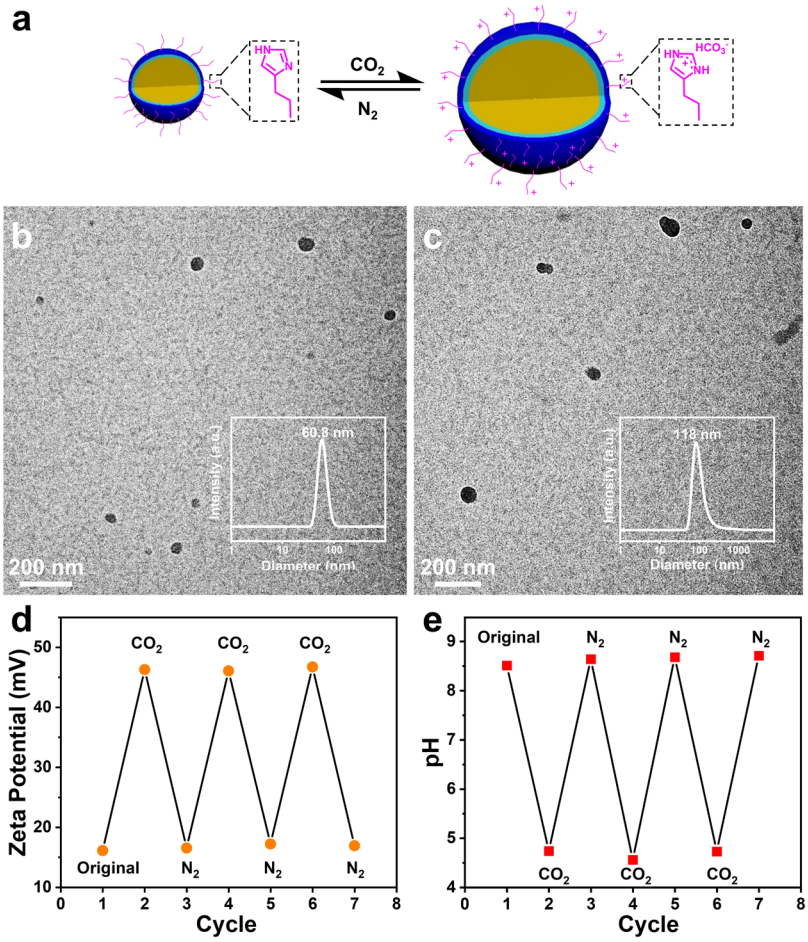

Figure 5. CO_2-responsive feature of spherical micelles. (a) Scheme of size variation for spherical micelles upon the alternating bubbling with CO_2 and N_2 gases. (b–e) Structural characterizations of spherical micelles bubbling with CO_2 for 30 min. (b) TEM image of initial small spherical micelles. The inset is the corresponding DLS curve. (c) TEM image of a CO_2-induced large spherical micelles. The inset is the corresponding DLS curve. (d) Zeta potential changes of the spherical micelle aqueous solution. (e) pH changes of the spherical micelle aqueous solution.

transition (Figure 3b,c). Upon irradiation with UV light (365 nm) for 3 h, all of the UTPNFs were transformed into spherical micelles (Figure 3b). The statistical average diameter of these spherical micelles was measured to be 61.4 ± 5.4 nm (Figure 3c). Such a significant transition was ascribed to the molecular conformation change of the azobenzene moiety from the rigid *trans*-form to the flexible *cis*-form, subsequently resulting in an increase toward polarity and flexibility and a decrease toward hydrophobicity of azobenzene-containing side chains at the microscopic level. As such, the curvature of the AAPs was successively increased, eventually leading to a notable macroscopic structural transition from UTPNFs to spherical micelles. Notably, the augment in diameter of spherical micelles was attributed to the formation of multi-micelle aggregates (MMAs) that resulted from the aggregation of small micelles through intermicellar associations.[45] Following the addition of good solvent (THF) and sequential irradiation with visible light (450 nm) for 3 h, the azobenzene units were reverted into a rigid *trans*-form, ultimately leading to the recovery of UTPNFs (Figure 3d). To further substantialize the occurrence of the photoisomerization phenomenon during the reversible structural transformation process, time-dependent UV–vis spectra of AAPs in THF or UTPNFs in aqueous solution (Figure 3e,f and Figure S8) were elaborately acquired to demonstrate the photoresponsive feature. Under UV irradiation, the peak at 304 nm assignable to the $\pi-\pi^*$ transition of *trans*-azobenzene gradually decreased, accompanied by a progressive increase toward the peak at 433 nm corresponding to the $n-\pi^*$ transition of *cis*-azobenzene (Figure 3e). These changes demonstrated the emergence of UV-triggered molecular conformation transition of N_{azo} units from the *trans*- to *cis*-form. Oppositely, subsequent irradiation with visible light resulted in the reversible trends of these two peaks (Figure 3f), suggesting the recovery of the *trans*-form azobenzene. Of note, the photoisomerization rate toward molecular conformational transition of the azobenzene moiety from the *trans*- to *cis*-form was much faster than that of the structural transformation from UTPNFs to spherical micelles (Figure 3g), and vice versa.

3.3. CO_2-Responsive Feature of UTPNFs. The pH-dependent reversible protonation of histamine units also endows the relative nanomaterials with a reversible CO_2-responsive performance. Therefore, these as-prepared UTPNFs may undergo a reversible size transition upon alternating bubbling with CO_2 or N_2 gases (Figure 4a). TEM and AFM were employed to validate the CO_2-triggered size variation of UTPNFs after bubbling with CO_2 (20 mL min^{-1}) into a UTPNF aqueous solution for 30 min (Figure 4b,c). Under the treatment with CO_2 flow, both TEM image (Figure 4b) and AFM image (Figure 4c and Figure S9) proved

https://doi.org/10.1021/acs.biomac.5c00211
Biomacromolecules 2025, 26, 2750–2758

that these aggregates were still the fiber-like nanostructures. Based on the AFM height image (inset of Figure 4c), the diameter of the newly produced UTPNFs was increased to ∼2.39 nm, which was larger than that of the original UTPNFs. Such a phenomenon was attributable to the protonation of the imidazole group with CO_2 and the resulting increase in the surface positive charges of UTPNFs, subsequently enhancing the electrostatic repulsion and thus leading to the swelling of UTPNFs. To prove our guess, the zeta potential and pH values of the UTPNF aqueous solution were meticulously evaluated to trace the reversible performance change upon alternating bubbling with CO_2 and N_2 gases. As shown in Figure 4d and Figure S10, the zeta potential value of the UTPNF aqueous solution was changed from +36.6 to +51.0 mV after CO_2-induced protonation. Conversely, the zeta potential value was recovered to +36.6 mV after the N_2-induced deprotonation. Moreover, the gases-triggered reversible change of the zeta potential values was maintained for at least three times of recyclable bubbling. Additionally, the pH value of the UTPNF aqueous solution was reversibly transitioned from 9.0 to 5.0 during the alternating bubbling treatment, capable of attractively reversible change for at least three times recycling (Figure 4e). Therefore, recyclable performance variations on both the zeta potential and pH values demonstrated the reversible CO_2-responsive capacity of UTPNFs.

3.4. CO_2-Responsive Feature of Spherical Micelles. Apart from the UTPNFs, the exterior histamine groups also endowed UV-induced spherical micelles with a relevant CO_2-response feature, leading to a reversible size transition under alternating bubbling with CO_2 and N_2 gases (Figure 5a). Before bubbling with CO_2 gas, the TEM image proved the formation of uniform spherical micelles after UV irradiation (Figure 5b), with a diameter of ∼61 nm measured by DLS (inset of Figure 5b). Upon treatment with CO_2 flow for 30 min, spherical micelles with a diameter of ∼118 nm were significantly crafted according to the TEM and DLS characterizations (Figure 5c). Owing to the protonation of histamine groups, the increasing electrostatic repulsion interaction was accountable for the swelling of small spherical micelles into big ones. Moreover, N_2-induced deprotonation was beneficial for reducing the electrostatic interactions, consequently resulting in a recovery of large spherical micelles (∼72 nm, Figure S11). Except for the size transition, the zeta potential and pH values were capable of a reversible change from +16.1 to +46.3 mV (Figure 5d and Figure S12) and from 8.5 to 4.7 (Figure 5e) during the alternating bubbling with CO_2 and N_2 gases, respectively. Of note, the zeta potential change amplitude of spherical micelles (∼30.2 mV) was 2 times greater than that of UTPNFs (∼14.4 mV), indicating the larger degree of protonation and subsequent stronger electrostatic repulsion. Additionally, the photoisomerization resulted in a molecular conformation transition from the rigid *trans*-form azobenzene to the flexible *cis*-form azobenzene, destroying the structural regularity and crystalline ability. Both the stronger electrostatic repulsion interaction and the low crystallinity within the spherical micelles were accountable for the 2 times greater size expansion toward spherical micelles. Therefore, all of these reversible changes were attributable to CO_2-induced protonation and N_2-induced deprotonation of histamine groups within the AAPs, respectively.

4. CONCLUSIONS

In summary, we presented a feasible bottom-up approach for generating photo/CO_2 dual stimuli-responsive 1.8 nm UTPNFs at a micrometer-scale level using the self-assembly of sequence-defined amphiphilic alternating peptoids. Based on the pendant hydrophobic conjugate stacking mechanism, the diameter of UTPNFs was highly dictated by the microscopic order packing of the suspended hydrophilic/hydrophobic side chains. The phototriggered transformation from UTPNFs to spherical micelles was rendered by the photoisomerization of azobenzene units of AAPs. Additionally, the CO_2-responsive capacity of both UTPNFs and spherical micelles was demonstrated by the reversible transitions in diameter, pH, and zeta potential values, which were attributable to the CO_2-induced protonation and N_2-induced deprotonation. Our work opens a promising avenue for the rational development of ultrathin organic nanofibers with dual stimuli-responsiveness.

■ ASSOCIATED CONTENT

Supporting Information

The Supporting Information is available free of charge at https://pubs.acs.org/doi/10.1021/acs.biomac.5c00211.

Details including materials, synthesis, self-assembly, and characterization of peptoids (PDF)

■ AUTHOR INFORMATION

Corresponding Authors

Xiaoling Yang − *Shanghai Key Laboratory of Advanced Polymeric Materials, Frontiers Science Center for Materiobiology and Dynamic Chemistry, School of Materials Science and Engineering, East China University of Science and Technology, Shanghai 200237, China*; Email: xlyang@ecust.edu.cn

Haibao Jin − *Shanghai Key Laboratory of Advanced Polymeric Materials, Frontiers Science Center for Materiobiology and Dynamic Chemistry, School of Materials Science and Engineering, East China University of Science and Technology, Shanghai 200237, China*; orcid.org/0000-0001-7777-8337; Email: haibaojin@ecust.edu.cn

Shaoliang Lin − *Shanghai Key Laboratory of Advanced Polymeric Materials, Frontiers Science Center for Materiobiology and Dynamic Chemistry, School of Materials Science and Engineering, East China University of Science and Technology, Shanghai 200237, China*; orcid.org/0000-0003-3374-9934; Email: slin@ecust.edu.cn

Authors

Mingyu Ding − *Shanghai Key Laboratory of Advanced Polymeric Materials, Frontiers Science Center for Materiobiology and Dynamic Chemistry, School of Materials Science and Engineering, East China University of Science and Technology, Shanghai 200237, China*

Qianyu Jiang − *Shanghai Key Laboratory of Advanced Polymeric Materials, Frontiers Science Center for Materiobiology and Dynamic Chemistry, School of Materials Science and Engineering, East China University of Science and Technology, Shanghai 200237, China*

Pengchao Wu − *Shanghai Key Laboratory of Advanced Polymeric Materials, Frontiers Science Center for Materiobiology and Dynamic Chemistry, School of Materials Science and Engineering, East China University of Science and Technology, Shanghai 200237, China*

https://doi.org/10.1021/acs.biomac.5c00211
Biomacromolecules 2025, 26, 2750−2758

Pengliang Sui − *Shanghai Key Laboratory of Advanced Polymeric Materials, Frontiers Science Center for Materiobiology and Dynamic Chemistry, School of Materials Science and Engineering, East China University of Science and Technology, Shanghai 200237, China*

Zichao Sun − *Shanghai Key Laboratory of Advanced Polymeric Materials, Frontiers Science Center for Materiobiology and Dynamic Chemistry, School of Materials Science and Engineering, East China University of Science and Technology, Shanghai 200237, China*

Complete contact information is available at: https://pubs.acs.org/10.1021/acs.biomac.5c00211

Notes

The authors declare no competing financial interest.

■ ACKNOWLEDGMENTS

Financial support was provided by the National Natural Science Foundation of China (52373114 and 52325308). The authors thank the Research Center of Analysis and Test of East China University of Science and Technology for the help on the UPLC-MS characterization.

■ REFERENCES

(1) Huang, C.; Soenen, S. J.; Rejman, J.; Lucas, B.; Braeckmans, K.; Demeester, J.; De Smedt, S. C. Stimuli-responsive electrospun fibers and their applications. *Chem. Soc. Rev.* **2011**, *40* (5), 2417−2434.

(2) Huang, Y.; Song, J.; Yang, C.; Long, Y.; Wu, H. Scalable manufacturing and applications of nanofibers. *Mater. Today* **2019**, *28*, 98−113.

(3) Freeman, R.; Han, M.; Álvarez, Z.; Lewis, J. A.; Wester, J. R.; Stephanopoulos, N.; McClendon, M. T.; Lynsky, C.; Godbe, J. M.; Sangji, H.; Luijten, E.; Stupp, S. I. Reversible self-assembly of superstructured networks. *Science* **2018**, *362* (6416), 808−813.

(4) Wang, L.; He, X.; Hao, Y.; Zheng, M.; Wang, R.; Yu, J.; Qin, X. Rational design of stretchable and highly aligned organic/inorganic hybrid nanofiber films for multidirectional strain sensors and solar-driven thermoelectrics. *Sci. China Mater.* **2023**, *66* (2), 707−715.

(5) Jochum, F. D.; Theato, P. Temperature- and light-responsive smart polymer materials. *Chem. Soc. Rev.* **2013**, *42* (17), 7468−7483.

(6) Stuart, M. A. C.; Huck, W. T. S.; Genzer, J.; Müller, M.; Ober, C.; Stamm, M.; Sukhorukov, G. B.; Szleifer, I.; Tsukruk, V. V.; Urban, M.; Winnik, F.; Zauscher, S.; Luzinov, I.; Minko, S. Emerging applications of stimuli-responsive polymer materials. *Nat. Mater.* **2010**, *9* (2), 101−113.

(7) Sato, O. Dynamic molecular crystals with switchable physical properties. *Nat. Chem.* **2016**, *8* (7), 644−656.

(8) Zhao, Y. S.; Fu, H.; Peng, A.; Ma, Y.; Liao, Q.; Yao, J. Construction and Optoelectronic Properties of Organic One-Dimensional Nanostructures. *Acc. Chem. Res.* **2010**, *43* (3), 409−418.

(9) Xue, J.; Xie, J.; Liu, W.; Xia, Y. Electrospun Nanofibers: New Concepts, Materials, and Applications. *Acc. Chem. Res.* **2017**, *50* (8), 1976−1987.

(10) Zhu, S.; Wang, S.; Huang, Y.; Tang, Q.; Fu, T.; Su, R.; Fan, C.; Xia, S.; Lee, P. S.; Lin, Y. Bioinspired structural hydrogels with highly ordered hierarchical orientations by flow-induced alignment of nanofibrils. *Nat. Commun.* **2024**, *15* (1), 118.

(11) Zupančič, Š.; Rijavec, T.; Lapanje, A.; Petelin, M.; Kristl, J.; Kocbek, P. Nanofibers with Incorporated Autochthonous Bacteria as Potential Probiotics for Local Treatment of Periodontal Disease. *Biomacromolecules* **2018**, *19* (11), 4299−4306.

(12) Nilawar, S.; Yadav, P.; Jain, N.; Saini, D. K.; Chatterjee, K. Protective Role of Nanoceria-Infused Nanofibrous Scaffold toward Bone Tissue Regeneration with Senescent Cells. *Biomacromolecules* **2024**, *25* (7), 4074−4086.

(13) Song, Q.; Wu, P.; Liu, F.; Sun, Z.; Jiang, C.; Gao, L.; Chen, J.; Jin, H.; Lin, J.; Lin, S. Ultrathin Polymer Nanotubes Assembled from Side-Chain Amphiphilic Alternating Azocopolymers for the Potential of Highly-Efficient and Photo-Controllable Dye Removal. *Macromolecules* **2024**, *57* (12), 5892−5901.

(14) Wang, C.; O'Hagan, M. P.; Li, Z.; Zhang, J.; Ma, X.; Tian, H.; Willner, I. Photoresponsive DNA materials and their applications. *Chem. Soc. Rev.* **2022**, *51* (2), 720−760.

(15) Xu, W.; Liu, C.; Liang, S.; Zhang, D.; Liu, Y.; Wu, S. Designing Rewritable Dual-Mode Patterns using a Stretchable Photoresponsive Polymer via Orthogonal Photopatterning. *Adv. Mater.* **2022**, *34* (31), No. 2202150.

(16) Sun, Z.; Zhu, L.; Liu, J.; Liu, F.; Wu, P.; Sui, P.; Jin, H.; Lin, S. Azobenzene-based ultrathin peptoid nanoribbons for the potential on highly efficient artificial light-harvesting. *Sci. China Chem.* **2024**, *67* (5), 1680−1686.

(17) Kim, J.; Park, J.; Jung, K.; Kim, E. J.; Tan, Z.; Xu, M.; Lee, Y. J.; Ku, K. H.; Kim, B. J. Light-Responsive Shape- and Color-Changing Block Copolymer Particles with Fast Switching Speed. *ACS Nano* **2024**, *18* (11), 8180−8189.

(18) Park, J.; Pramanick, S.; Park, D.; Yeo, J.; Lee, J.; Lee, H.; Kim, W. J. Therapeutic-Gas-Responsive Hydrogel. *Adv. Mater.* **2017**, *29* (44), No. 1702859.

(19) Darabi, A.; Jessop, P. G.; Cunningham, M. F. CO_2-responsive polymeric materials: synthesis, self-assembly, and functional applications. *Chem. Soc. Rev.* **2016**, *45* (15), 4391−4436.

(20) Yan, Q.; Zhou, R.; Fu, C.; Zhang, H.; Yin, Y.; Yuan, J. CO_2-Responsive Polymeric Vesicles that Breathe. *Angew. Chem., Int. Ed.* **2011**, *50* (21), 4923−4927.

(21) Zhuang, J.; Gordon, M. R.; Ventura, J.; Li, L.; Thayumanavan, S. Multi-stimuli responsive macromolecules and their assemblies. *Chem. Soc. Rev.* **2013**, *42* (17), 7421−7435.

(22) Mu, R.; Zhu, D.; Abdulmalik, S.; Wijekoon, S.; Wei, G.; Kumbar, S. G. Stimuli-responsive peptide assemblies: Design, self-assembly, modulation, and biomedical applications. *Bioact. Mater.* **2024**, *35*, 181−207.

(23) Lin, S.; Shang, J.; Theato, P. Facile Fabrication of CO_2-Responsive Nanofibers from Photo-Cross-Linked Poly(pentafluorophenyl acrylate) Nanofibers. *ACS Macro Lett.* **2018**, *7* (4), 431−436.

(24) Chen, L.; Liu, R.; Yan, Q. Polymer Meets Frustrated Lewis Pair: Second-Generation CO_2-Responsive Nanosystem for Sustainable CO_2 Conversion. *Angew. Chem., Int. Ed.* **2018**, *57* (30), 9336−9340.

(25) Jiang, L.; Mei, X.; Shao, T.; Yang, X.; Long, W.; Wan, M.; Fan, Y.; Xiong, J.; Zhang, X.; Hu, Y.; Gu, H.; Wang, Z. Flexible and self-powered blinking and eyeball movements sensing based on electrospun lead-free piezoelectric nanofibers. *Sci. China Mater.* **2024**, *67* (12), 3948−3955.

(26) Chen, L.; Mei, S.; Fu, K.; Zhou, J. Spinning the Future: The Convergence of Nanofiber Technologies and Yarn Fabrication. *ACS Nano* **2024**, *18* (24), 15358−15386.

(27) Nishiguchi, A.; Araki, E.; Palai, D.; Ito, S.; Taguchi, T. Development of Phase-Separating Microfiber Network Hydrogels to Promote In Vitro Vascularization. *Biomacromolecules* **2024**, *25* (9), 6146−6154.

(28) Xue, J.; Wu, T.; Dai, Y.; Xia, Y. Electrospinning and Electrospun Nanofibers: Methods, Materials, and Applications. *Chem. Rev.* **2019**, *119* (8), 5298−5415.

(29) Shi, X.; Zuo, Y.; Zhai, P.; Shen, J.; Yang, Y.; Gao, Z.; Liao, M.; Wu, J.; Wang, J.; Xu, X.; Tong, Q.; Zhang, B.; Wang, B.; Sun, X.; Zhang, L.; Pei, Q.; Jin, D.; Chen, P.; Peng, H. Large-area display textiles integrated with functional systems. *Nature* **2021**, *591* (7849), 240−245.

(30) Allard, C.; Alvarez, L.; Bantignies, J.-L.; Bendiab, N.; Cambré, S.; Campidelli, S.; Fagan, J. A.; Flahaut, E.; Flavel, B.; Fossard, F.; Gaufrès, E.; Heeg, S.; Lauret, J.; Loiseau, A.; Marceau, J.; Martel, R.; Marty, L.; Pichler, T.; Voisin, C.; Reich, S.; Setaro, A.; Shi, L.;

Wenseleers, W. Advanced 1D heterostructures based on nanotube templates and molecules. *Chem. Soc. Rev.* **2024**, *53* (16), 8457−8512.
(31) Yang, F.; Zhao, X.; Xue, T.; Yuan, S.; Huang, Y.; Fan, W.; Liu, T. Superhydrophobic polyvinylidene fluoride/polyimide nanofiber composite aerogels for thermal insulation under extremely humid and hot environment. *Sci. China Mater.* **2021**, *64* (5), 1267−1277.
(32) Jin, H.; Wu, P.; Liu, Z.; Sun, Z.; Feng, W.; Ding, Y.; Cao, H.; Lin, Z.; Lin, S. Robust Multifunctional Ultrathin 2 Nanometer Organic Nanofibers. *ACS Nano* **2024**, *18* (32), 21576−21584.
(33) Liao, Y.; Loh, C. H.; Tian, M.; Wang, R.; Fane, A. G. Progress in electrospun polymeric nanofibrous membranes for water treatment: Fabrication, modification and applications. *Prog. Polym. Sci.* **2018**, *77*, 69−94.
(34) Chen, J.; Yu, C.; Shi, Z.; Yu, S.; Lu, Z.; Jiang, W.; Zhang, M.; He, W.; Zhou, Y.; Yan, D. Ultrathin Alternating Copolymer Nanotubes with Readily Tunable Surface Functionalities. *Angew. Chem., Int. Ed.* **2015**, *54* (12), 3621−3625.
(35) Shao, Q.; Zhang, S.; Hu, Z.; Zhou, Y. Multimode Self-Oscillating Vesicle Transformers. *Angew. Chem., Int. Ed.* **2020**, *59* (39), 17125−17129.
(36) Xu, Q.; Yu, C.; Jiang, L.; Wang, Y.; Liu, F.; Jiang, W.; Zhou, Y. Coacervate-Assisted Polymerization-Induced Self-Assembly of Chiral Alternating Copolymers into Hierarchical Bishell Capsules with Sub-5 nm Ultrathin Lamellae. *Small Methods* **2023**, *7* (12), No. 2300136.
(37) Li, Z.; Cai, B.; Yang, W.; Chen, C. L. Hierarchical Nanomaterials Assembled from Peptoids and Other Sequence-Defined Synthetic Polymers. *Chem. Rev.* **2021**, *121* (22), 14031−14087.
(38) Mannige, R. V.; Haxton, T. K.; Proulx, C.; Robertson, E. J.; Battigelli, A.; Butterfoss, G. L.; Zuckermann, R. N.; Whitelam, S. Peptoid nanosheets exhibit a new secondary-structure motif. *Nature* **2015**, *526* (7573), 415−420.
(39) Robertson, E. J.; Battigelli, A.; Proulx, C.; Mannige, R. V.; Haxton, T. K.; Yun, L.; Whitelam, S.; Zuckermann, R. N. Design, Synthesis, Assembly, and Engineering of Peptoid Nanosheets. *Acc. Chem. Res.* **2016**, *49* (3), 379−389.
(40) Liu, J.; Cai, B.; Cui, L.; Chen, C. L. Peptoid-based hierarchically-structured biomimetic nanomaterials: Synthesis, characterization and applications. *Sci. China Mater.* **2020**, *63* (7), 1099−1112.
(41) Jin, H.; Ding, Y. H.; Wang, M.; Song, Y.; Liao, Z.; Newcomb, C. J.; Wu, X.; Tang, X. Q.; Li, Z.; Lin, Y.; Yan, F.; Jian, T.; Mu, P.; Chen, C. L. Designable and dynamic single-walled stiff nanotubes assembled from sequence-defined peptoids. *Nat. Commun.* **2018**, *9* (1), 270.
(42) Wu, P.; Sui, P.; Peng, G.; Sun, Z.; Liu, F.; Yao, W.; Jin, H.; Lin, S. Designable Photo-Responsive Micron-Scale Ultrathin Peptoid Nanobelts for Enhanced Performance on Hydrogen Evolution Reaction. *Adv. Mater.* **2024**, *36* (16), No. 2312724.
(43) Wu, P.; Sui, P.; Xu, Z.; Zhu, L.; Jia, Y.; Dai, S.; Jin, H.; Lin, S. 1D Ultrathin Peptoid Nanobelts-Based Organic-Inorganic Nanocomposite for Photo-Controllable Chemo-Enzymatic Cascade Catalysis. *Adv. Funct. Mater.* **2024**, *34* (48), No. 2408583.
(44) Zhu, X.; Zhang, D.; Liu, F.; Wu, P.; Jin, H.; Lin, S. Self-assembly and photo-responsive behavior of sequence-defined amphiphilic azobenzene alternating peptoids. *Acta Polym. Sin.* **2025**, *56* (1), 104−113.
(45) Qi, M.; Zhou, Y. Multimicelle aggregate mechanism for spherical multimolecular micelles: from theories, characteristics and properties to applications. *Mater. Chem. Front.* **2019**, *3* (10), 1994−2009.

https://doi.org/10.1021/acs.biomac.5c00211
Biomacromolecules 2025, 26, 2750−2758